Quantitative characterizations of ultrashort echo (UTE) images for supporting air–bone separation in the head

You may also be interested in:

Quantitative characterizations of ultrashort echo (UTE) images for supporting air–bone separation in the head

Shu-Hui Hsu[1]**, Yue Cao**[1,2,3]**, Theodore S Lawrence**[1]**, Christina Tsien**[1]**, Mary Feng**[1]**, David M Grodzki**[4] **and James M Balter**[1,3]

[1] Department of Radiation Oncology, University of Michigan, Ann Arbor, MI 48109 USA
[2] Department of Radiology, University of Michigan, Ann Arbor, MI 48109 USA
[3] Department of Biomedical Engineering, University of Michigan, Ann Arbor, MI 48109 USA
[4] Magnetic Resonance, Siemens AG, Erlangen, Germany

E-mail: shuihsu@umich.edu, yuecao@med.umich.edu, tsl@med.umich.edu, ctsien@med.umich.edu, maryfeng@med.umich.edu, david.grodzki@siemens.com and jbalter@med.umich.edu

CrossMark

Abstract

Accurate separation of air and bone is critical for creating synthetic CT from MRI to support Radiation Oncology workflow. This study compares two different ultrashort echo-time sequences in the separation of air from bone, and evaluates post-processing methods that correct intensity nonuniformity of images and account for intensity gradients at tissue boundaries to improve this discriminatory power. CT and MRI scans were acquired on 12 patients under an institution review board-approved prospective protocol. The two MRI sequences tested were ultra-short TE imaging using 3D radial acquisition (UTE), and using pointwise encoding time reduction with radial acquisition (PETRA). Gradient nonlinearity correction was applied to both MR image volumes after acquisition. MRI intensity nonuniformity was corrected by vendor-provided normalization methods, and then further corrected using the N4itk algorithm. To overcome the intensity-gradient at air–tissue boundaries, spatial dilations, from 0 to 4 mm, were applied to threshold-defined air regions from MR images. Receiver operating characteristic (ROC) analyses, by comparing predicted (defined by MR images) versus 'true' regions of air and bone (defined by CT images), were performed with and without residual bias field correction and local spatial expansion. The post-processing corrections increased the areas under the ROC curves (AUC) from 0.944 ± 0.012 to 0.976 ± 0.003 for UTE images, and from 0.850 ± 0.022

to 0.887 ± 0.012 for PETRA images, compared to without corrections. When expanding the threshold-defined air volumes, as expected, sensitivity of air identification decreased with an increase in specificity of bone discrimination, but in a non-linear fashion. A 1 mm air mask expansion yielded AUC increases of 1 and 4% for UTE and PETRA images, respectively. UTE images had significantly greater discriminatory power in separating air from bone than PETRA images. Post-processing strategies improved the discriminatory power of air from bone for both UTE and PETRA images, and reduced the difference between the two imaging sequences. Both post-processed UTE and PETRA images demonstrated sufficient power to discriminate air from bone to support synthetic CT generation from MRI data.

(Some figures may appear in colour only in the online journal)

1. Introduction

Cortical bone is invisible on conventional magnetic resonance images (MRI) due to its ultra-short T2 and T2* (Nyman *et al* 2008, Rank *et al* 2013). This presents challenges for attenuation correction of PET on a PET/MRI system, as well as for the use of MRI as a primary imaging modality for radiation treatment planning, as it requires identifying bone regions on MRI (Yin *et al* 1998, Zaidi *et al* 2003, Chen *et al* 2007, Stanescu *et al* 2008, Catana *et al* 2010, Keereman *et al* 2010, Greer *et al* 2011, Johansson *et al* 2011, Lambert *et al* 2011, Berker *et al* 2012, Dowling *et al* 2012, Kim *et al* 2012, Hsu *et al* 2013, Jonsson *et al* 2013, Kapanen and Tenhunen 2013, Rank *et al* 2013, Korhonen *et al* 2014, Uh *et al* 2014).

Recently, ultra-short echo time (UTE) pulse sequences with radial k-space sampling have been developed to visualize tissues with very short T2 and T2*, such as bone, tendons and ligaments (Robson *et al* 2003, Catana *et al* 2010, Keereman *et al* 2010). While these sequences improve the contrast between bone and air, a recent study indicates that image intensities of bone and air in the skull still overlap, leading to mislabeling the two using intensity thresholds (Hsu *et al* 2013). There are two major issues contributed to overlapping intensities of air and bone. First, intensities of uniform tissue compositions across the image volume are non-uniform ('bias field'), an observation which is usually attributed to RF-coil sensitivity variation across the field of view as well as gradient-driven eddy currents (Sled *et al* 1998). Although vendors provide on-line intensity correction (normalization) options, residual intensity non-uniformity still degrades air and bone discrimination as well as tissue classification. Secondly, there is an intensity-gradient at the air-tissue interface on the UTE images, which may be due to limitations in the base resolution, the number of spokes, and the chemical-shift effect in the radial sampling of the ultrashort TE sequences.

In this study, we investigated capabilities of two different ultrashort TE pulse sequences for separating air from bone. One is an ultrashort TE sequence (UTE) using 3D radial k-space sampling, which has been previously studied (Hsu *et al* 2013). Another is termed pointwise encoding time reduction with radial acquisition (PETRA), combining 3D radial sampling with Cartesian single point sampling in the center of the k-space (Grodzki *et al* 2012b). We also evaluated whether post-processing strategies, correcting residual intensity non-uniformity and dilating the threshold-derived air mask, could improve the discrimination between air and bone signals.

2. Methods and materials

2.1. Patients and image acquisitions

Twelve patients with intracranial tumors participated in an institution review board-approved prospective protocol, and underwent brain MRI and CT scans in radiation treatment configurations while immobilized using custom thermoplastic masks. All MRI and CT scans were performed on a large-bore 3 T MR scanner (Skyra, Siemens Medical Systems, Erlangen, Germany) and a CT simulator (Brilliance, Philips Medical Systems, Cleveland OH), respectively. MR images were acquired using a combination of an 18-channel anterior surface coil and either a posterior 4-channel surface coil or 4–12 channels of a 32-channel posterior spine coil. In the first seven patients, UTE images were acquired with TE/TR = 0.06/7.7 ms, flip angle =12°, voxel size ≈ 1.4 × 1.4 × 1.4 mm^3, 60 000 spokes and pre-scan normalization (online and vendor-provided) to reduce the bias field effect on images. In the last five patients, both UTE and PETRA images were acquired with voxel sizes ≈ 1.1 × 1.1 × 1.1 mm^3, and B1 normalization to test which online normalization, B1 versus pre-scan, can better reduce the bias field. The acquisition parameters of the PETRA images were TE/TR = 0.07/4.69 ms, 60 000 spokes and flip angle =6°. All MR images were corrected on-line for gradient non-linearity-caused spatial distortion. For CT acquisition, the whole brain region of these patients was scanned with slice thickness of 3 mm and in-plane pixel size ranging from 0.5 × 0.5 to 1 × 1 mm^2.

2.2. Image processing

2.2.1. Image registration.　CT images were aligned to corresponding MR images using mutual information-based rigid-body registration. All aligned image volumes were reformatted as stacks of axial slices with voxel sizes of 1 × 1 × 1 mm^3.

2.2.2. Bias field correction.　All MR images were corrected for residual intensity non-uniformity using a commonly applied post-processing bias-field correction algorithm (N4itk) (Tustison *et al* 2010) and implemented in a publicly available image analysis software environment (SLICER 3.6, surgical processing laboratory, Brigham and Women's Hospital, Boston, MA). The N4itk algorithm is based on nonparametric nonuniform intensity normalization (N3) (Sled *et al* 1998), with improvement in B-spline smoothing strategy and convergence performance. The bias field was estimated within the volume defined by the skin surface. The N4itk optimization parameters included: BSpline order of 3, BSpline grid resolutions of (1, 1, 1), a shrink factor of 2, a maximum number of 500 iterations at each of the 3 resolution levels, and a convergence threshold of 0.001.

2.2.3. MRI intensity scaling.　All UTE and PETRA image intensities before and after bias field correction were scaled to have the mean intensity for each image volume equal to 1000 within a volume bounded by the CT-defined external contour.

2.2.4. Air mask expansions.　In our previous work (Hsu *et al* 2013), an air mask within the skin surface was generated by thresholding UTE image intensities prior to tissue classifications. In this study, we investigated whether applying dilation to the threshold-defined air mask could yield a better separation of air and bone. To test this hypothesis, the threshold-defined air volumes from either UTE or PETRA images were dilated by 1, 2, 3 or 4 voxels (mm), and each of the resulting masks were evaluated.
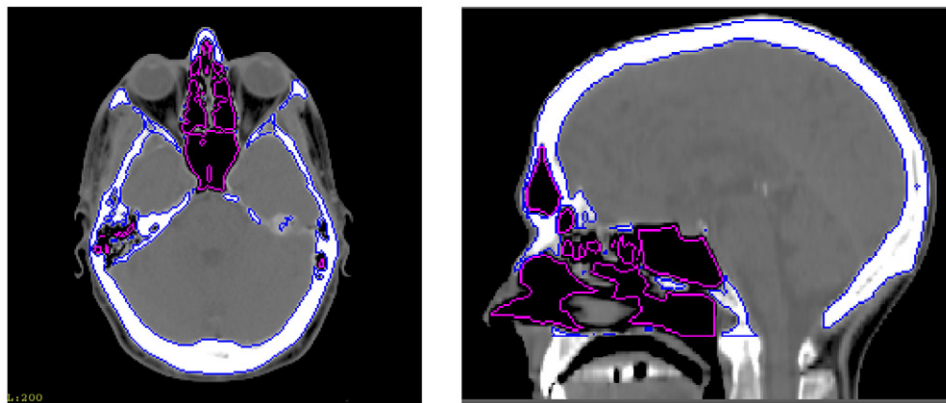
Figure 1. 'True' air (magenta) and bone (blue) regions generated from CT images using thresholds of < -400 HU and > 200 HU, respectively.

2.3. Evaluation of air–bone separation

Receiver operating characteristic (ROC) analysis was performed to evaluate sensitivity and specificity of separation of air from bone using UTE and PETRA images for the following scenarios: (1) using the vendor's pre-scan normalization versus B1 normalization, (2) without and with additional bias-field correction by N4itk, and (3) without and with spatial dilations of the threshold-defined air masks. CT images were used to define 'true' air (intensity < -400 HU) and 'true' bone (intensity > 200 HU) voxels in the head (figure 1). Intensity thresholds from 50 to 3050 were applied to the voxels within the regions of interest on the scaled UTE and PETRA images with and without bias-field correction to label air (intensities below the tested thresholds). For each given tested threshold, the true positive rate (sensitivity) was defined as the number of voxels co-labeled as air on both MRI and CT divided by the total number of air voxels from CT, and the false positive rate (1-specificity) was defined as the number of voxels labeled as air on MRI but defined as bone on CT divided by the total number of bone voxels from CT. By advancing the intensity thresholds from 50 to 3050, ROC curves were generated. To test the air mask dilation, ROC curves were generated similarly at each threshold for the expanded air mask.

2.4. Synthetic CT

To demonstrate how the post-processing strategies impact on the quality of MRI-derived CT, synthetic CT images of one patient were generated using the air masks created on UTE and PETRA images (using an intensity threshold of 350 on scaled images), with and without bias-field correction, and with spatial dilations (1 mm for UTE, 1 and 2 mm for PETRA). Creation of the synthetic CT was then performed according to the method described previously (Hsu *et al* 2013).

3. Results

3.1. Intensity uniformity correction

Intensity nonuniformity was observed in both UTE and PETRA images of the patients (figure 2). The spatial and magnitude extents of the bias fields calculated by N4itk varied
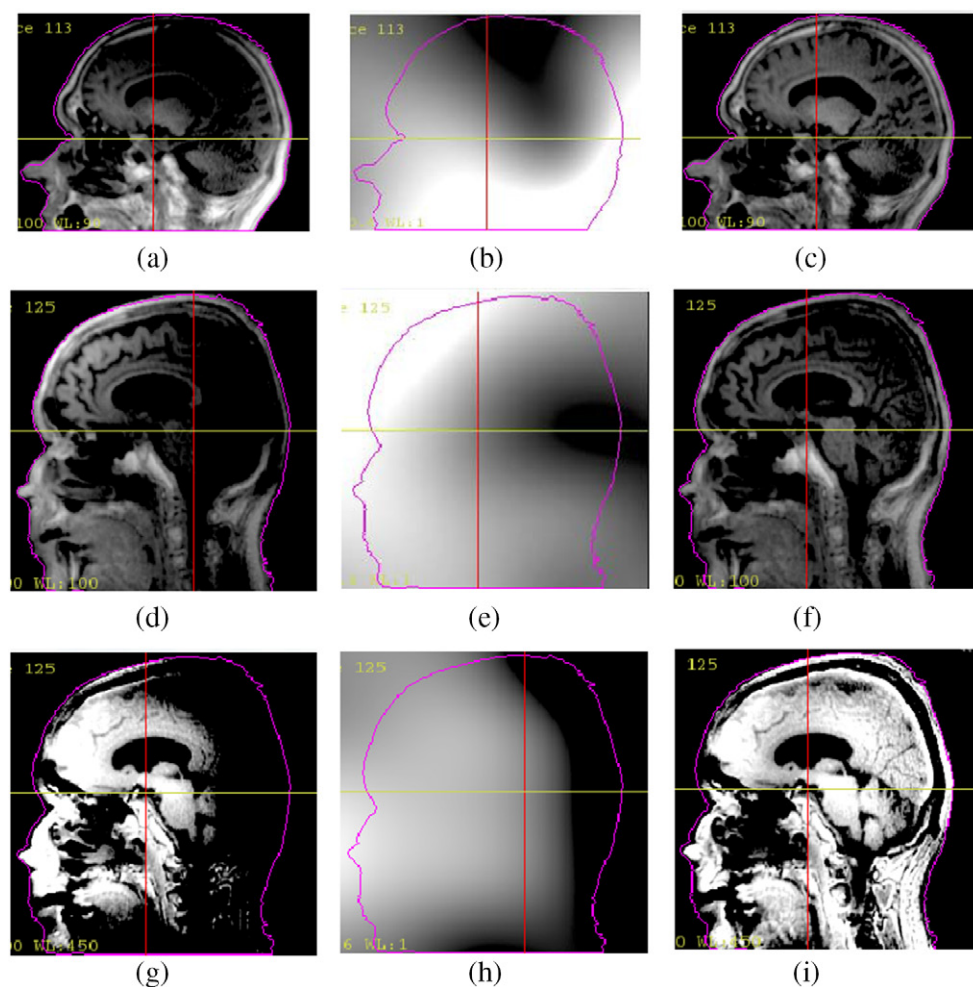
Figure 2. Uncorrected MR images (*a*, *d*, *g*), estimated bias fields using N4itk (*b*, *e*, *h*), and corrected MR images (*c*, *f*, *i*) of two patients. (*a*)–(*c*): UTE images acquired using pre-scan normalization on patient 1; (*d*)–(*f*): UTE images acquired using B1 normalization on patient 2; (*g*)–(*i*): PETRA images acquired using B1 normalization on patient 2. The images before and after using N4itk are windowed identically.

across patients, but low intensities were often observed in superior and/or posterior regions of the head. Pre-scan normalization resulted in different bias fields than B1 normalization when evaluated using N4itk (figures 2(*a*)–(*f*)). Correcting these bias fields by using N4itk reduced intensity variations in the brain regions of the MR images (figure 2).

Post-processing bias field correction improved the performance of UTE and PETRA images for separation of air from bone. The bias-corrected UTE and PETRA images yielded areas under the ROC curves (AUCs) of 0.976 ± 0.003 (Mean $\pm$ standard error) ($n = 12$) and 0.887 ± 0.012 ($n = 5$), respectively, which were greater than those (0.944 ± 0.012 and 0.850 ± 0.022) from the uncorrected images (figure 3 and table 1). The improvement in air masking when using N4itk to correct the bias field on the UTE images was significant ($p = 0.02$), but not on the PETRA images ($p = 0.1$). Also, the AUC for air masking using the bias-corrected UTE images was significantly greater than the similarly-processed PETRA
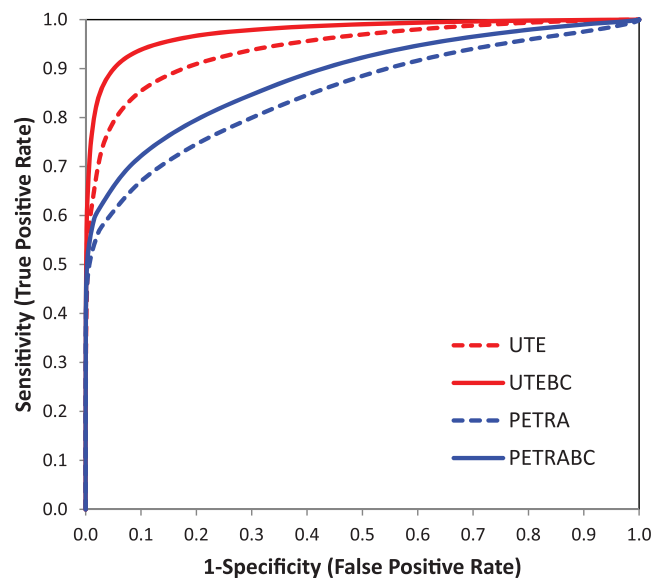
Figure 3. ROC curves of discrimination of air from bone using UTE (12 patients) and PETRA (5 patients) images without and with bias field correction (BC).

Table 1. AUC comparisons (mean ± standard error of mean) for UTE and PETRA images without and with bias field corrections as well as various spatial expansions (0–4 mm). Numbers of patients were 7 and 5 for group 1 (pre-scan normalization) and group 2 (B1 normalization), respectively.

MRI volumes	Dilations (mm)	AUC (UTE)			AUC (PETRA)
		Group 1 (7)	Group 2 (5)	Combined (12)	Group 2 (5)
No bias field correction	0	0.932 ± 0.020	0.960 ± 0.007	0.944 ± 0.012	0.850 ± 0.022
Bias field corrections	0	0.974 ± 0.004	0.978 ± 0.004	0.976 ± 0.003	0.887 ± 0.012
	1	0.987 ± 0.003	0.991 ± 0.001	0.989 ± 0.002	0.925 ± 0.008
	2	0.989 ± 0.003	0.991 ± 0.001	0.990 ± 0.002	0.941 ± 0.007
	3	0.988 ± 0.003	0.988 ± 0.001	0.988 ± 0.002	0.948 ± 0.007
	4	0.986 ± 0.003	0.984 ± 0.001	0.985 ± 0.002	0.951 ± 0.007

images ($p = 0.007$), suggesting that UTE images have greater power to discriminate air from bone (table 1).

The relationships between image intensity thresholds and sensitivity and specificity for discriminating air from bone are explicitly revealed in figure 4. It can be seen that increasing the intensity threshold for air masking to 350 improves sensitivity with minimal loss of specificity on UTE images, and a threshold of 260 would similarly maximize sensitivity with minimal specificity loss for PETRA.

ROC curves for UTE scans using different normalizations are shown in figure 5. Air masks from UTE images acquired using B1 normalization had an AUC of 0.960 ± 0.007, which was 3% better but not significantly different than masks extracted from images acquired using pre-scan normalization ($p = 0.2$). Post-processing bias-field correction using N4itk improved the AUCs to 0.974 ± 0.004 and 0.978 ± 0.004 for masks extracted from the pre-scan and B1-normalized images, respectively. These curves were also insignificantly different ($p = 0.5$),
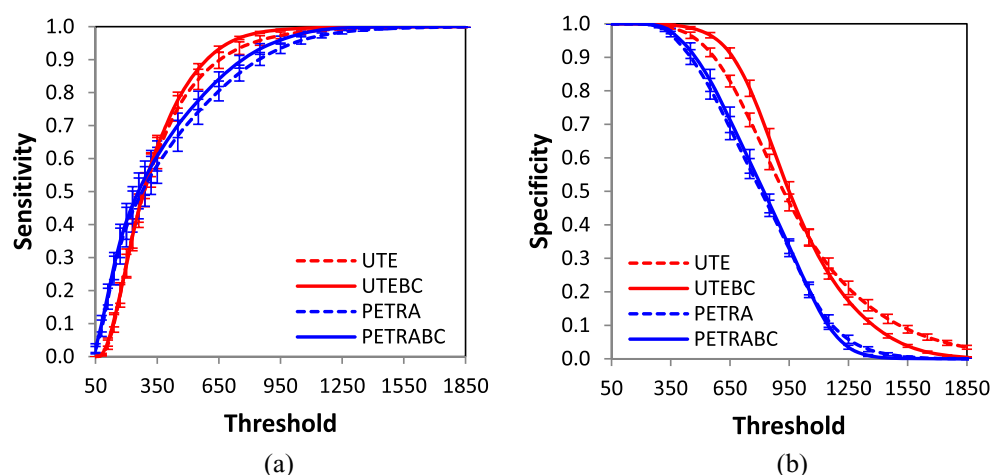
Figure 4. (*a*) Sensitivity versus threshold and (*b*) specificity versus threshold for UTE and PETRA images without and with bias field corrections. The error bars represent standard errors of the means.

indicating that post-processing improved air-bone separation but did not elucidate any difference between B1 normalization and pre-scan normalization in performing this separation.

3.2. Dilation of air masks

Figure 6 illustrates the changes in air mask definitions due to dilation. It can be seen that small dilations generally help fill air cavities, but larger dilations eventually include too many tissue voxels in the air mask, thus diminishing specificity. Dilating the air masks by 1 mm significantly improved the AUCs by 1% ($p < 0.001$) and 4% ($p < 0.01$) for the UTE and PETRA images, respectively (figure 7 and table 1). Dilating the air masks by 2 mm yielded no significant improvement in the AUC over the 1 mm expansion for the UTE images, but led to a 2% increase in the AUC for the PETRA images which was significant ($p = 0.04$). For dilations larger than 2 mm, sensitivity, most notably at high specificity, deteriorated quickly for both UTE and PETRA images, even though the AUC values still increased using dilated masks for PETRA images.

Plotting the sensitivity and specificity as a function of intensity thresholds in figure 8 reveals that the 1 mm dilation of the air masks in the UTE and PETRA images causes an increase in sensitivity with a decrease in specificity over the whole threshold range. However, at relatively low thresholds, the benefit of the increase in sensitivity could overcome the negligible decrease in specificity (e.g. thresholds <550 and 350 for UTE and PETRA, respectively).

3.3. Synthetic CT using corrected air masks

Figure 9 shows examples of synthetic CT images generated using the modified air masks. The impact of bias field correction is most notable when applied to the PETRA images for air masking, see figure 9(*f*), in which the large section of posterior skull mislabeled as air in figure 9(*e*) is mostly resolved by the bias field correction (arrows). The positive impact of dilation is most visible in figure 9(*d*) with a 1 mm expansion on the mask of the bias-corrected UTE image improving resolution of the anterior sinus (arrows), while the negative impacts of dilation are most visible in figure 9(*h*), where mislabeled air in the posterior skull is significantly expanded (arrows).
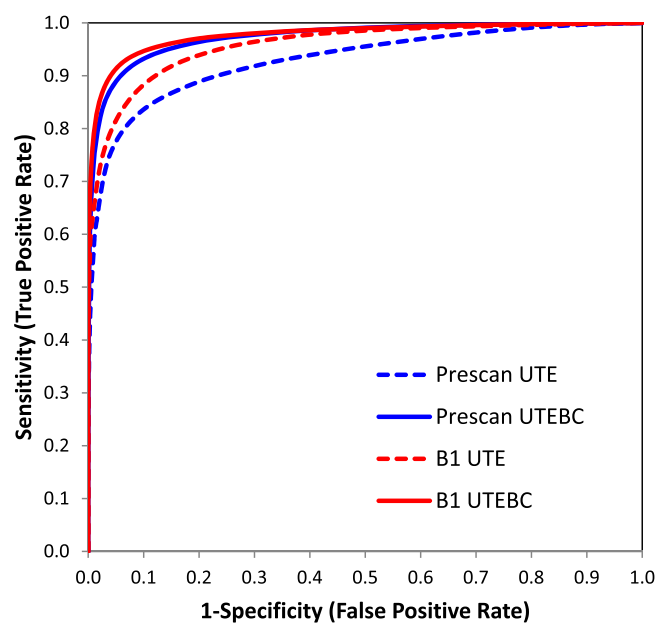
Figure 5. ROC curves of air and bone discrimination from UTE images with two different normalization methods, pre-scan (7 patients) and B1 (5 patients), applied during image acquisition. Solid lines represent the curves with additional bias-field correction.
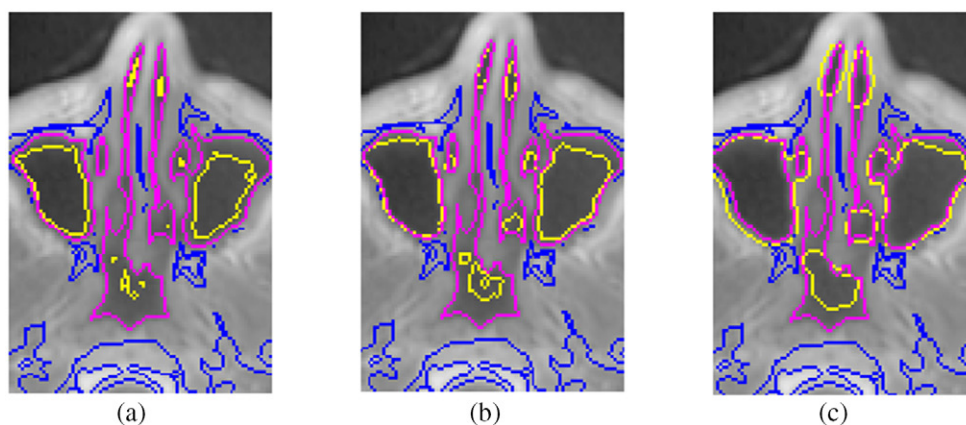

Figure 6. 'True' air (magenta) and bone (blue) regions in the nasal cavity as well as air masks (yellow) dilated by (*a*) 0 (no dilations), (*b*) 1 and (*c*) 3 mm after applying a threshold of 350 on the bias-field corrected and normalized UTE images.

4. Discussion

This study explored ultrashort TE scanning techniques, normalization methods, and post-processing techniques for separating air from bone. Overall observations were that UTE performed better than PETRA, and that post-processing using bias field correction techniques as well as small spatial expansions of threshold-defined masks could improve the performance of both UTE as well as PETRA for separating air and bone. Understanding the impacts of thresholds on specificity and sensitivity separately helps guide intelligent decisions on selecting thresholds on intensity-normalized images.
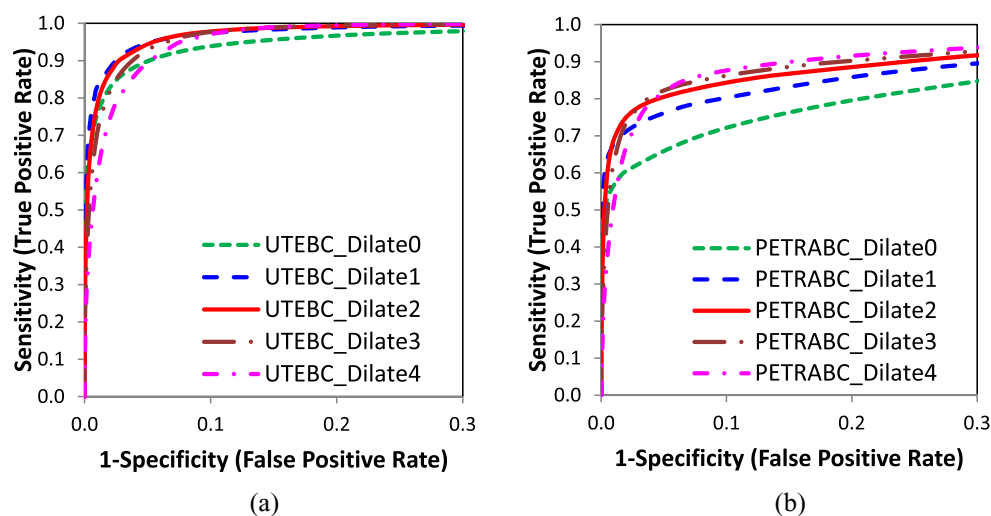
Figure 7. ROC curves of air and bone discrimination using UTE and PETRA images with bias field corrections and with various spatial expansions (from 0 to 4 mm). The curves are shown at high specificities (0.7–1.0) to emphasize reductions in sensitivity with increasing expansion.
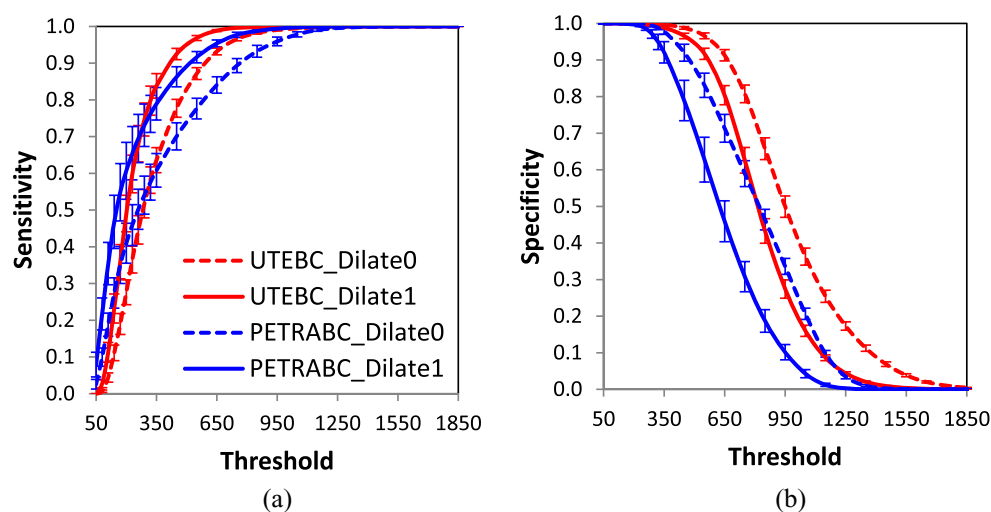

Figure 8. (*a*) Sensitivity versus threshold and (*b*) specificity versus threshold for air–bone separation from UTE (12 patients) and PETRA (5 patients) images without and with 1 mm mask dilation. The error bars represent standard errors of mean.

Both UTE (Robson *et al* 2003) and PETRA pulse sequences use 3D radial sampling in k-space and enable detection of MR signals from ultrashort TE species like bones and ligaments. The major difference between the two sequences is that the radial sampling gradients are switched on before and during RF excitation in the PETRA sequence. Thus, there are some limitations for the excitation for PETRA: (1) it cannot be slice-selective and must be non-selective, (2) bandwidth must be high enough in order not to have unwanted slice selection (Grodzki *et al* 2012a), and thus (3) the flip-angle is limited to somewhere below 6–10° with something like a 1 mm resolution on a clinical scanner. This also limits the contrast more to proton density, but
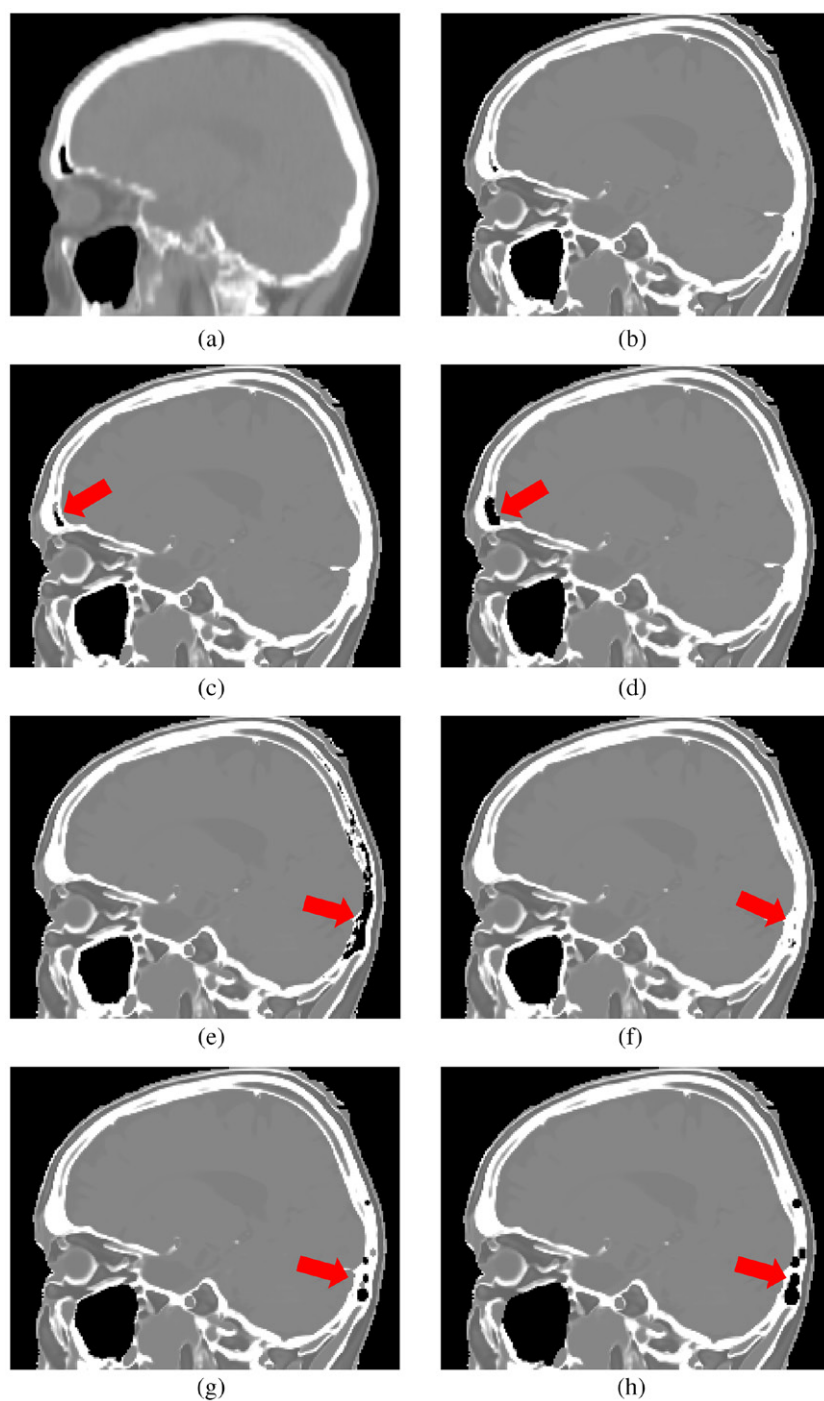
Figure 9. (*a*) CT and (*b*)–(*h*) synthetic CT from seven different air masks generated by: (*b*) UTE images, (*c*) bias-corrected UTE images, (*d*) bias-corrected UTE images with a 1 mm expansion, (*e*) PETRA images, (*f*) bias-corrected PETRA images, (*g*) bias-corrected PETRA images with a 1 mm expansion, and (*h*) bias-corrected PETRA images with a 2 mm expansion.

not too much T1 weighted. The UTE sequence does not have such limitations, as the imaging gradients are only switched on after the excitation for the radial sampling (potentially leading to artifacts from other factors including eddy-currents and time-delays). Thus, higher flip-angles with higher T1-contrast, higher readout-bandwidths, and slice-selection could be used with UTE. Both sequences have the chemical shift effect in the radial direction.

These differences between UTE and PETRA may in part explain their differences in separating bone and air. For PETRA, the gradients are turned on prior to excitation, which may lead to radially rotated slice excitations and artifacts (Grodzki *et al* 2012a). Although the artifacts and rotated slice excitations are mitigated by using low gradients, small flip angles, and post-processing correction, they may still cause imperfect intensities and intensity blurring at the tissue boundaries. Other causes of blurring in both UTE as well as PETRA may be the number of spokes used and chemical shift of fat signals. The selection of coils for coverage of the patients' heads may also have led to artifacts that impacted the contrast in various regions of the head, as UTE as implemented in our system has oversampling, while PETRA does not.

While post-processing bias field correction was applied to individual image volumes, it is important to note that the algorithm employed (N4itk) uses image intensity uniformity and does not account for the physical factors impacting bias fields. These factors are roughly constant across all scans taken in a single session without coil or patient adjustment, and thus improved bias field estimation may be possible by simultaneous estimation across multiple images acquired for synthetic CT generation. Future studies will investigate the potential of simultaneous bias field estimation from multiple images to further improve air-bone estimation as well as synthetic CT generation.

5. Conclusions

Post-processing tools to improve the discrimination between air and bone have been evaluated for both UTE and PETRA images. Two different forms of intensity normalization at the scanner failed to completely remove bias fields, and correcting the estimated residual bias fields improved air–bone discrimination. Applying appropriate expansions (1–2 mm) to threshold-defined air regions further improved separation of air and bone for both UTE and PETRA images. This study indicates that both bias field correction as well as spatial dilation of threshold-extracted air masks would be of benefit for synthetic CT generation from MRI to support treatment planning and image guidance in radiation oncology.

Acknowledgments

References

Berker Y *et al* 2012 MRI-based attenuation correction for hybrid PET/MRI systems: a 4-class tissue segmentation technique using a combined ultrashort-echo-time/Dixon MRI sequence *J. Nucl. Med.* **53** 796–804

Catana C, van der Kouwe A, Benner T, Michel C J, Hamm M, Fenchel M, Fischl B, Rosen B, Schmand M and Sorensen A G 2010 Toward implementing an MRI-based PET attenuation-correction method for neurologic studies on the MR-PET brain prototype *J. Nucl. Med.* **51** 1431–8

Chen L, Nguyen T B, Jones E, Chen Z, Luo W, Wang L, Price R A Jr, Pollack A and Ma C M 2007 Magnetic resonance-based treatment planning for prostate intensity-modulated radiotherapy: creation of digitally reconstructed radiographs *Int. J. Radiat. Oncol. Biol. Phys.* **68** 903–11

Dowling J A, Lambert J, Parker J, Salvado O, Fripp J, Capp A, Wratten C, Denham J W and Greer P B 2012 An atlas-based electron density mapping method for magnetic resonance imaging (MRI)-alone treatment planning and adaptive MRI-based prostate radiation therapy *Int. J. Radiat. Oncol. Biol. Phys.* **83** e5–11

Greer P B, Dowling J A, Lambert J A, Fripp J, Parker J, Denham J W, Wratten C, Capp A and Salvado O 2011 A magnetic resonance imaging-based workflow for planning radiation therapy for prostate cancer *Med. J. Aust.* **194** S24–7

Grodzki D M, Jakob P M and Heismann B 2012a Correcting slice selectivity in hard pulse sequences *J. Magn. Reson.* **214** 61–7

Grodzki D M, Jakob P M and Heismann B 2012b Ultrashort echo time imaging using pointwise encoding time reduction with radial acquisition (PETRA) *Magn. Reson. Med.* **67** 510–8

Hsu S H, Cao Y, Huang K, Feng M and Balter J M 2013 Investigation of a method for generating synthetic CT models from MRI scans of the head and neck for radiation therapy *Phys. Med. Biol.* **58** 8419–35

Johansson A, Karlsson M and Nyholm T 2011 CT substitute derived from MRI sequences with ultrashort echo time *Med. Phys.* **38** 2708–14

Jonsson J H, Johansson A, Soderstrom K, Asklund T and Nyholm T 2013 Treatment planning of intracranial targets on MRI derived substitute CT data *Radiother. Oncol.* **108** 118–22

Kapanen M and Tenhunen M 2013 T1/T2*-weighted MRI provides clinically relevant pseudo-CT density data for the pelvic bones in MRI-only based radiotherapy treatment planning *Acta Oncol.* **52** 612–8

Keereman V, Fierens Y, Broux T, De Deene Y, Lonneux M and Vandenberghe S 2010 MRI-based attenuation correction for PET/MRI using ultrashort echo time sequences *J. Nucl. Med.* **51** 812–8

Kim J H, Lee J S, Song I C and Lee D S 2012 Comparison of segmentation-based attenuation correction methods for PET/MRI: evaluation of bone and liver standardized uptake value with oncologic PET/CT data *J. Nucl. Med.* **53** 1878–82

Korhonen J, Kapanen M, Keyrilainen J, Seppala T and Tenhunen M 2014 A dual model HU conversion from MRI intensity values within and outside of bone segment for MRI-based radiotherapy treatment planning of prostate cancer *Med. Phys.* **41** 011704

Lambert J *et al* 2011 MRI-guided prostate radiation therapy planning: investigation of dosimetric accuracy of MRI-based dose planning *Radiother. Oncol.* **98** 330–4

Nyman J S, Ni Q, Nicolella D P and Wang X 2008 Measurements of mobile and bound water by nuclear magnetic resonance correlate with mechanical properties of bone *Bone* **42** 193–9

Rank C M, Tremmel C, Hunemohr N, Nagel A M, Jakel O and Greilich S 2013 MRI-based treatment plan simulation and adaptation for ion radiotherapy using a classification-based approach *Radiat. Oncol.* **8** 51

Robson M D, Gatehouse P D, Bydder M and Bydder G M 2003 Magnetic resonance: an introduction to ultrashort TE (UTE) imaging *J. Comput. Assist. Tomogr.* **27** 825–46

Sled J G, Zijdenbos A P and Evans A C 1998 A nonparametric method for automatic correction of intensity nonuniformity in MRI data *IEEE Trans. Med. Imaging* **17** 87–97

Stanescu T, Jans H S, Pervez N, Stavrev P and Fallone B G 2008 A study on the magnetic resonance imaging (MRI)-based radiation treatment planning of intracranial lesions *Phys. Med. Biol.* **53** 3579–93

Tustison N J, Avants B B, Cook P A, Zheng Y, Egan A, Yushkevich P A and Gee J C 2010 N4ITK: improved N3 bias correction *IEEE Trans. Med. Imaging* **29** 1310–20

Uh J, Merchant T E, Li Y, Li X and Hua C 2014 MRI-based treatment planning with pseudo CT generated through atlas registration *Med. Phys.* **41** 051711

Yin F F, Gao Q, Xie H, Nelson D F, Yu Y, Kwok W E, Totterman S, Schell M C and Rubin P 1998 MR image-guided portal verification for brain treatment field *Int. J. Radiat. Oncol. Biol. Phys.* **40** 703–11

Zaidi H, Montandon M L and Slosman D O 2003 Magnetic resonance imaging-guided attenuation and scatter corrections in 3D brain positron emission tomography *Med. Phys.* **30** 937–48